RSC Advances

PAPER

View Article Online
View Journal | View Issue

Cite this: *RSC Adv.*, 2022, **12**, 20672

Investigation of the soft carbon microstructure in silicon/carbon anodes for superior lithium storage†

Juntao Du, *[a] Jiangkai Ma,[ab] Zetao Liu,[ac] Wenchao Wang,[ac] Huina Jia,[a] Minxin Zhang[a] and Yi Nie *[ad]

It is essential to consider the controllable microstructure of soft carbon and its enhancement effect on the electrochemical performance of silicon (Si) active materials. In this study, a series of Si@mesocarbon microbead (Si@MCMB) composites were prepared using mesophase pitch as the soft carbon source to coat nano-Si. The results showed that the ordered carbon layer stacking of soft carbon increased slightly with increasing heat treatment temperature in the range of 800–1400 °C. The Si@MCMB composites at higher temperature had a turbostratic carbon layer texture with rich porosity and smaller specific surface area, and had good cycle stability and high rate performance. These results highlighted that the co-existing structure of turbostratic carbon arrays with abundant porosity from soft carbon, provided the electron/ion transfer channels, underwent Si alloy volume change and enhanced the mechanical stability. Importantly, the relationship between the capacity retention rate of the Si@MCMB anodes and the microstructural characteristics (carbon layer and porosity) of soft carbon was established, which provided effective guidance for the design of high-performance silicon/carbon (Si/C) anode materials.

Received 28th March 2022
Accepted 12th July 2022

DOI: 10.1039/d2ra01997c

rsc.li/rsc-advances

1. Introduction

Lithium-ion batteries (LIBs) are one of the development directions of new energy technologies. Si/C composites represent some of the most promising anode materials to break through the application bottleneck of high specific energy LIBs.[1] The properties of active Si particles have higher requirements of carbon composition, so the design of carbon structures has become a research hotspot in the area of Si/C anode materials.[2,3] Soft carbon contains controllable disorder and graphitic regions, endowing a high storage capacity and good cycling stability, and is one of the most promising carbon materials used in Si/C anodes.[4] The main technical problem is that it is difficult to control the microstructure of soft carbon and its influence on the electrochemical behavior of active Si particles is not clear.[5,6] Although challenging, it is vital to understand how the controllable microstructure of soft carbon efficiently improves the electrochemical performance of Si/C composite anodes.

Mesophase pitch as soft carbon contains ordered graphite regions with controllable crystallinity, which imparts excellent electron transfer properties and structural elasticity to improve electrochemical performance.[7,8] Firstly, the streamlined carbon arrays of mesophase pitch after carbonization have moderately expanded layer spacing, enabling them to have better rate performance than hard carbons and conventional graphite anodes.[9,10] Additionally, compared with hard carbon, the pores and defects of mesophase pitch can be easily adjusted by the heat treatment temperature to achieve a reasonable compromise between ion diffusion and electrolyte compatibility. Its relatively dense structure tends to result in higher vibration density and volumetric energy density.[11,12] In particular, the microstructure of mesophase pitch is greatly affected by the heat treatment temperature, which is a potential method for optimizing the electrochemical performance of active Si and needs to be further explored.[13] However, a clear correlation between the order degree of mesophase pitch as soft carbon and the corresponding lithium storage at a carbonization temperature of 1000–1400 °C is still elusive, and the enhancement effect of microstructure on the electrochemical behavior of active Si is not clear.

Here, we synthesized a series of Si/C composites with a regularly adjusted microstructure through the gradual carbonization of mesophase pitch as soft carbon from 800 to 1400 °C. The lithium storage behavior and related structural stability of soft carbon and the enhancement effect of its microstructure on the electrochemical behavior of active Si were studied using the prepared materials. Based on our previous report,[14] this study further focused on the design of the turbostratic carbon layer arrays and pore structure of soft carbon

[a]Zhengzhou Institute of Emerging Industrial Technology, Zhengzhou, 450000, China. E-mail: jtdu@ipezz.ac.cn
[b]Zhengzhou University, Zhengzhou 450000, China
[c]Dalian University of Technology, Dalian, 116024, China
[d]Institute of Process Engineering, Chinese Academy of Sciences, Beijing 100190, China. E-mail: ynie@ipe.ac.cn

† Electronic supplementary information (ESI) available. See https://doi.org/10.1039/d2ra01997c

by finely adjusting the heat treatment temperature. The correlation between the microstructural characteristics of soft carbon and the electrochemical behavior of Si/C composites was systematically explored.

2. Experimental

2.1 Synthesis of Si@MCMB

The coal-based mesophase pitch (CMP) was prepared from coal tar pitch in our laboratory and its properties are listed in Tables S1 and S2.† Nano-Si particles with an average diameter of 100 nm were purchased from Gexin Nano Technology Co., Ltd, Shanghai, China. The CMP and nano-Si (100 nm) in a mass ratio of 100 : 15 to obtain a Si/CMP composite in a tube furnace at 400 °C for 2 h. Si/CMP mixture and silicone oil in a mass ratio of 1 : 100 were sealed off in a stainless-steel reactor at 300 °C for 1 h and the reactor was then rapidly cooled to room temperature. The Si@MCMB composites was separated by centrifugation, washed with petroleum ether until colorless and then dried at 80 °C in a vacuum for 12 h. Finally, the Si@MCMB composites were obtained by pre-oxidation at 300 °C in air for 1 h and carbonized from 800 to 1400 °C for 2 h in an argon atmosphere before being labeled as Si@MCMB-8, Si@MCMB-10, Si@MCMB-12, Si@MCMB-13 and Si@MCMB-14, respectively. Similarly, the MCMB samples with different heat treatment temperatures from 800 to 1400 °C were labeled as MCMB-8, MCMB-10, MCMB-12, MCMB-13 and MCMB-14, respectively.

2.2 Materials characterization

The morphology of the samples was observed by scanning electron microscopy (SEM). Carbonized samples were embedded in a thermosetting resin, which was then cut with a sharp scalpel after curing, allowing for observation of the internal structure of the samples through their cross section by SEM and energy-dispersive X-ray spectroscopy (EDS). The crystal structures of the samples were examined using X-ray diffraction (XRD) with Cu-Kα radiation. The graphitization degrees of the different samples were analyzed using a LabRAM HR Raman spectrometer. The Si content in samples was obtained by thermogravimetric analysis (TGA) operated from 30 to 900 °C at a heating rate of 10 °C min^{-1} under an air atmosphere. The specific surface area was determined according to the Brunauer–Emmett–Teller (BET) method and the pore size distribution was derived from the Barrett–Joyner–Halenda model using an ASAP2020HD88 apparatus (USA).

2.3 Electrochemical performance evaluation

The electrochemical performance of the Si@MCMB composites was evaluated using coin-type half cells, with lithium foil as a counter electrode. The anode materials were fabricated by mixing the active materials, acetylene black and poly(vinylidene fluoride) in a mass ratio of 8 : 1 : 1 by ball milling at 150 rpm for 2 h. Then, the copper foil after coating was dried at 100 °C for 12 h under a vacuum, and punched into a circular electrode with a diameter of 14 mm as the working electrode. A polypropylene film (Celgard 2400) was utilized as the separator, and a solution of $LiPF_6$ (1.0 mol L^{-1}) in dimethyl carbonate and ethylene carbonate (mass ratio 1 : 1) was treated as electrolyte. A LAND battery testing system was used to measure the cycling and rate performance of the anodes. Cyclic voltammetry (CV) was carried out using an electrochemical workstation (CHI660E, CH Instruments, China) at a scan rate of 0.1 mV s^{-1} from 0.01 to 3.0 V. Electrochemical impedance spectroscopy (EIS) was conducted in a frequency range from 100 kHz to 0.01 Hz.

3. Results and discussion

3.1 Structural characteristics

The morphology and cross section of the Si@MCMB composites were identified by SEM (Fig. 1 and S1†). The Si@MCMB composite particles were uniform in size and uniformly dispersed, as shown in Fig. S1.† Fig. 1 shows that the Si@MCMB composites exhibited a near-spherical structure with a diameter of 30–40 μm and the nano-Si particles were well embedded in the cross section of the Si@MCMB composites. Furthermore, the elemental mapping images in Fig. S2† also suggested that the nano-Si particles were well encapsulated in MCMB. With increasing heat treatment temperature, the cross sections of Si@MCMB gradually showed different degrees of laminar cracking and shrinkage, which may be due to the volatilization of the light components of MCMB or the polymerization and rearrangement of the carbon layers.[15] Mesophase pitch forms a curved carbon layer stacked structure under high-temperature carbonization and the external nano-Si particles may cause distortion and gap in the carbon layer texture.[16–18] Moreover, the Si@MCMB composites showed an ordered carbon layer texture and abundant void space, which may provide efficient transport channels for electrons and lithium ions and accommodate the volume change of Si.[19,20]

As shown in Fig. 2a, five distinct diffraction peaks at 28.5°, 47.2°, 56.2°, 69.2° and 76.3° could be observed, which are assigned to the (111), (220), (311), (400) and (331) planes of Si (JCPDS 27-1402), respectively. In addition, the weak peak at 25° could be attributed to the (002) plane of the carbon materials.[21] It is noteworthy that the formation of major impurities such as SiC and SiO_2 species in Si@MCMB-13 was mainly ascribed to

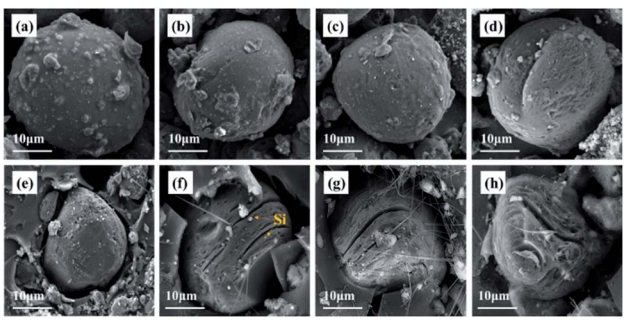

Fig. 1 SEM images of morphology and cross sections: Si@MCMB-8 (a and e); Si@MCMB-10 (b and f); Si@MCMB-12 (c and g); Si@MCMB-13 (d and h).

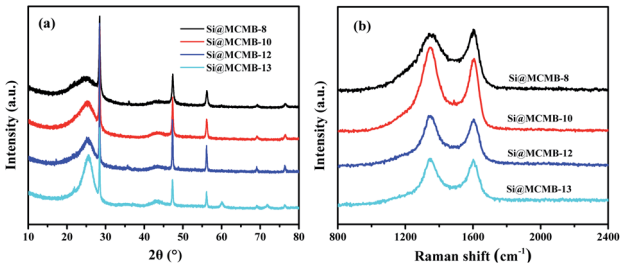

Fig. 2 XRD pattern (a) and Raman spectra (b) of Si@MCMB composites.

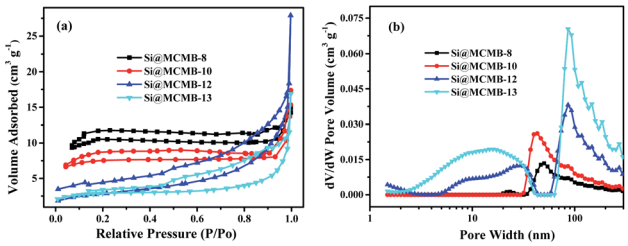

Fig. 3 N_2 adsorption–desorption isotherm (a) and pore-size distribution curves (b) of Si@MCMB composites.

the carbon and oxygen element of mesophase pitch (Fig. S4†). The inert SiC and SiO_2 seriously affected the transfer of electron ions between the Si core and carbon shell, as confirmed in the subsequent electrochemical performance. As listed in Table 1, the carbon structure parameters could be calculated from XRD.[22] The Si@MCMB composites showed a decrease in the interlayer spacing (d_m) and an increase in the crystallite sizes (L_a and L_c) with the heat treatment temperature increasing from 800 to 1300 °C. The presence of a strong peak at 1350 cm^{-1} and a weak peak at 1605 cm^{-1} in Fig. 2b were recognized as the disorder D band and graphitic G band of the carbon materials, respectively. It is well-known that the intensity ratio (I_D/I_G) is used to reflect the order degree of carbon materials.[23] The I_D/I_G values were calculated to be 1.156, 1.131, 1.086 and 1.067 for Si@MCMB-8, Si@MCMB-10, Si@MCMB-12 and Si@MCMB-13, respectively, as listed in Table 1. It can be found that the carbon layer order degree of the latter two was obviously better than for the former two.

The Si contents in Si@MCMB composites were measured by TGA, as shown in Fig. S3.†[24] The Si contents in Si@MCMB-8, Si@MCMB-10, Si@MCMB-12 and Si@MCMB-13 were estimated as 15.8 wt%, 16.1 wt%, 16.4 wt% and 16.8 wt%, respectively. In contrast, the weight loss of Si@MCMB-8 and Si@MCMB-10 started at 500 °C and that of Si@MCMB-12 and Si@MCMB-13 started at 650 °C, which also indicated the escape of the light components in the latter two by carbonization at the higher temperature.

The N_2 adsorption–desorption isotherm and pore-size distribution curves of the Si@MCMB composites are shown in Fig. 3. Interestingly, with the heat treatment temperature increasing from 800 to 1300 °C, the BET specific surface area showed a decreasing trend while the total pore volume showed an increasing trend, as presented in Table 1. This phenomenon may be caused by the different number of pores in the Si@MCMB composites in the mesoporous and macroporous areas, respectively. Compared to the values of 31.069 $m^2\ g^{-1}$ and 0.015 $cm^3\ g^{-1}$ of Si@MCMB-8, the BET specific surface area (S_{BET}) and pore volume of Si@MCMB-13 were 8.454 $m^2\ g^{-1}$ and 0.038 $cm^3\ g^{-1}$, respectively. Generally, when the heat treatment temperature was less than 1000 °C, the oxygen in the form of CO_2 and CO and light components escaped to form part of the pores. Concomitantly, above 1000 °C, the H_2 release and carbon layer rearrangement of the mesophase pitch form a turbostratic carbon layer structure and created pores.[25,26] Notably, the changes in pore distribution and carbon texture affected the lithium storage process and channels, and the aromatic ring compound and heteroatoms affected the active point of lithium storage.[11,27]

Furthermore, the structure parameter of carbon layers and hierarchical porosity about Si@MCMB composites was listed in Table 1. The reasonable design of the porosity in the carbon matrix is beneficial for improving the electrochemical performance of Si/C electrodes, which provided efficient active sites and electron/ion diffusion paths.[28,29] This differential determination of the Si@MCMB composites may reflect their different electrochemical properties.

Table 1 Structural parameters of Si@MCMB composites

Si@MCMB-*X*	8	10	12	13
Interlayer spacing d_m/nm	0.3551	0.3486	0.3472	0.3455
Crystallite sizes L_a/nm	7.93	8.35	9.63	13.59
Stacking height L_c/nm	3.53	4.90	5.04	7.67
Disordered degree I_D/I_G	1.156	1.131	1.086	1.067
$S_{BET}/m^2\ g^{-1}$	31.069	20.419	9.884	8.454
Pore volume/$cm^3\ g^{-1}$	0.015	0.018	0.023	0.038

3.2 Electrochemical performance

Fig. 4 show the charge/discharge curves for the Si@MCMB composites. In the initial cycle, the Si@MCMB anodes had

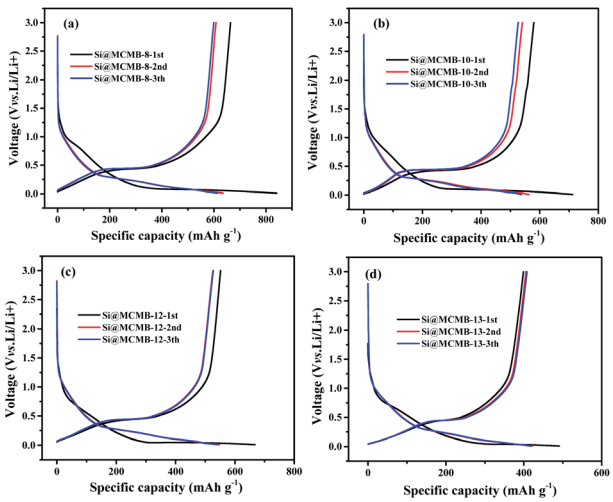

Fig. 4 Charge/discharge curves of the Si@MCMB composites.

discharge capacities of 841.5, 712.2, 674.7 and 495.7 mA h g^{-1} for Si@MCMB-8, Si@MCMB-10, Si@MCMB-12 and Si@ MCMB-13, accompanied by initial coulombic efficiencies (ICEs) of 78.92%, 81.47%, 82.04% and 83.67%, respectively. In the first discharge, the smooth inclined line between 1.2 and 0.2 V corresponded to the SEI formation and lithium insertion in the carbon layers.[30] The flat plateau at ~0.15 V in the discharge process was assigned to the Li_xSi alloying reaction. The long plateau at ~0.4 V in the charge process originated from the Li-ion extraction.[19,22] The irreversible capacity loss of the first two Si@MCMB anodes was mainly caused by the large specific surface area, aromatic heteroatoms and carbon layer structure, which caused the formation process of the SEI to consume too much lithium. In contrast, the last two Si@MCMB anodes had smaller surface areas, fewer aromatic heteroatoms and abundant pore channels and thus their first coulombic efficiency was slightly better.

As shown in Fig. 5, the significant plateau of the Si@MCMB composites in the charging process at 0.3–0.5 V originated from the reversible Li_xSi delithiation process.[31,32] There was an evident peak at ~0.2 V in the discharge process, which was assigned to the Li_xSi alloying reaction. It was notable that the intensities of both the anodic and cathodic peaks gradually increased with further cycles, possibly due to the gradual activation process.[29] In comparison, the two relatively weak oxidation peaks at ~0.12 and 1.0 V could be attributed to Li-ion delithiation through stacked carbon layers, desorption from microvoids or structural defects in the carbon matrix, and reactions between Li ions and heteroatomic functional groups, respectively.[33,34] Furthermore, the distinct enhancement peak near 0 V for each Si@MCMB composite was associated with the reversible intercalation of Li ions into the stacked carbon layers and the structural defects in the form of nanopores and heteroatomic functional groups.[35] During the first cathode scanning process of each Si@MCMB composite, there was an irreversible reduction peak of the first cycles at 0.6–0.8 V, which was associated with the formation of an SEI on the electrode surface.[22,36]

As shown in Fig. 6a, the MCMB composites showed similar charge–discharge performance, which was consistent with the cycling performance (Fig. S5†). It was noted that the initial discharge capacity decreased gradually from MCMB-8 to MCMB-13 (Table S3†) and this was attributed to the change in the carbon layer stacked microstructure caused by the heat treatment temperature. MCMB-8 anode, as a hydrogen-containing disordered soft carbon, showed a larger initial specific capacity, but the subsequent irreversible capacity was presumably caused by the collapse of the carbon structure and the imperfect structure of the pores.[37] Furthermore, the Si@MCMB composites showed significant differences in irreversible capacity, with Si@MCMB-12 and Si@MCMB-13 showing relatively small losses (Table 2). This may be explained by the fact that the Si@MCMB-8 and Si@MCMB-10 composites had relatively larger specific surface areas, smaller pore volumes and a narrow pore distribution at ~50 nm (Tables 1 and S3†), which may cause the generation of the SEI and microporous lithium storage to consume too much lithium, resulting in a large irreversible capacity. This was also verified by the CV curves (Fig. 5).

As shown in Fig. 6b, the discharge capacity of the Si@MCMB-12 anode was up to 421.1 mA h g^{-1} after 200 cycles, which was higher than that of the Si@MCMB-8 anode (260.2 mA h g^{-1}) and Si@MCMB-10 anode (367.0 mA h g^{-1}) under the same conditions. The capacity retention rate of the Si@MCMB anodes from 800 to 1300 °C showed a different tendency in decrease after 200 cycles, exhibiting 39.18%, 63.25%, 76.08% and 93.20%, respectively (Fig. 6c and Table 2). Fig. 6d shows that the Si@MCMB-12 and Si@MCMB-13 anodes had better rate performance than Si@MCMB-8 and Si@MCMB-10, exhibiting high capacities at current densities of 0.2, 0.4, 0.8, 1.6 and 3.2 A g^{-1}, respectively. Furthermore, Si@MCMB-12 and Si@MCMB-13 had relatively smaller specific surface areas, abundant carbon layers stacked and pore volume distribution, which provided better conditions for SEI generation and

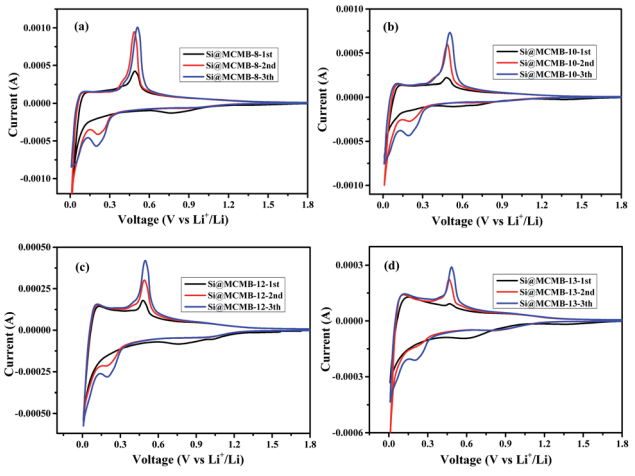

Fig. 5 CV curves of Si@MCMB composites.

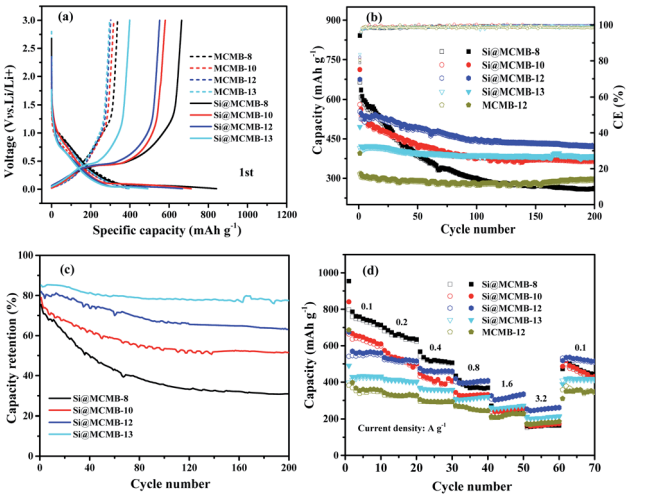

Fig. 6 First charge/discharge curves (a), cycling performance at 0.2 A g^{-1} (b), capacity retention rate (c) and rate performance (d).

Table 2 Electrochemical performance data for Si@MCMB anodes

Si@MCMB-*X* anodes	8	10	12	13
Reversible capacity/mA h g^{-1}	664.1	580.2	553.5	414.7
Irreversible capacity/mA h g^{-1}	177.4	132	121.2	81.0
ICE/%	78.92	81.47	82.04	83.67
Capacity after 200 cycles/mA h g^{-1}	260.2	367	421.1	386.5
Capacity retention rate/%	39.18	63.25	76.08	93.20

electron/ion channels.[7,13] In addition, the abundant pore volume distribution was beneficial to buffer the volume change of the Si alloying process, ensuring the mechanical stability of the anodes. Therefore, the Si@MCMB-12 and Si@MCMB-13 anodes showed good cycling and rate properties, as listed in Tables 1 and 2.

The first CV curves and EIS plots of the Si@MCMB anodes are illustrated in Fig. 7. By comparing the first CV curves of the Si@MCMB anodes, it could be found that the cathodic and anodic peaks become weaker with the heat treatment temperature from 800 to 1300 °C, while the charge transfer resistance (R_{ct}) was gradually increased in the EIS plots (Table S4†). This phenomenon was attributed to Si@MCMB-8 and Si@MCMB-10 having larger specific surface areas, pore-size distribution (~50 nm) and high interlayer spacing with poor order degree structures, which were all conducive to the contact between the electrode surface and the electrolyte and even lithium-ion diffusion.[38] In contrast, the larger impedance of the Si@MCMB-12 and Si@MCMB-13 anodes may be attributed to the close packing of the electrode materials, small specific surface areas and pore-size distribution (<30 and >60 nm, respectively). The relatively weak alloying process may be caused by the poor contact conductivity of the coated carbon parent and the contact points about the silicon–carbon interface decrease because of the increased disorder of the carbon layer.[39,40] Therefore, it was noteworthy that Si@MCMB-12 and Si@MCMB-13 anodes still showed good cyclic stability and high rate performance, probably due to the enhancement effect of structural stability, pore distribution and carbon layer structure, which offset the negative factors of higher impedance and weaker alloying.

The relationship between the electrochemical performance and structural characteristics for the Si@MCMB composites was further analyzed. SEM images revealed the morphological changes of the Si@MCMB anodes (mass loading 1.1 mg cm^{-2}) after 200 cycles (Fig. 8). The apparent morphology of the Si@MCMB-12 and Si@MCMB-13 anodes had a smoother surface with fewer cracks in their electrode coating, indicating that the anode structures maybe still maintain relative integrity after 200 cycles.[24,41] Significantly, the good structural integrity and stability was attributed to the turbostratic carbon layer structure and pore volume buffer space, which might facilitate the diffusion of electrolyte ions and alleviate the volume change of active Si particles during the lithium storage process.[42]

Based on the above results, the improved cycling stability and excellent rate performance of the Si@MCMB-12 and Si@MCMB-13 anodes may be attributed to the turbostratic carbon layer texture and pore volume buffer space. After 200 cycles, the capacity retention rate of the Si@MCMB composite anodes had a positive correlation with porosity and carbon layer order degree, while the specific surface area was the opposite, as shown in Fig. 9. Firstly, the carbon layer spacing and void volume could well accommodate the volume charge of Si during charge and discharge. Secondly, the nano-Si particles were well

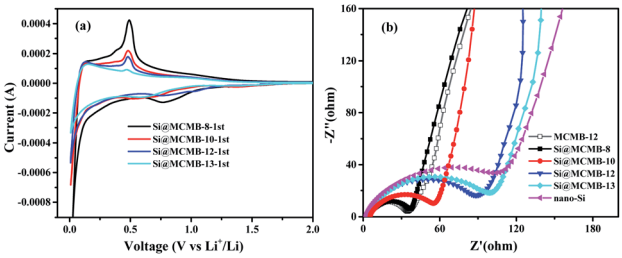

Fig. 7 First CV curves of Si@MCMB anodes (a) and EIS plots of Si@MCMB, nano-Si and MCMB-12 anodes (b).

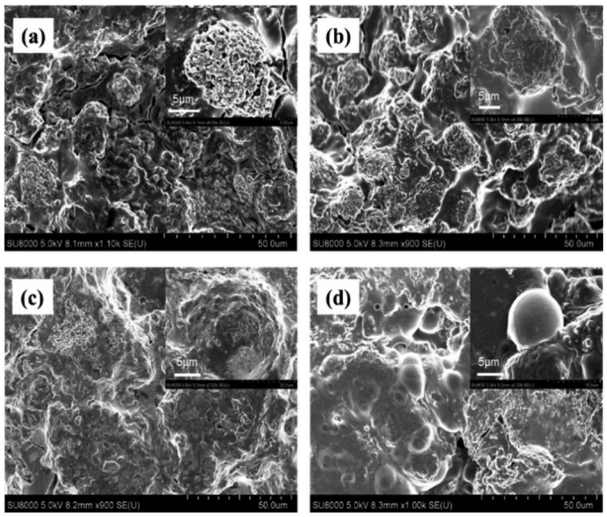

Fig. 8 SEM images of Si@MCMB-8 (a), Si@MCMB-10 (b), Si@MCMB-12 (c) and Si@MCMB-13 (d) anodes after 200 cycles at 0.2 A g^{-1}.

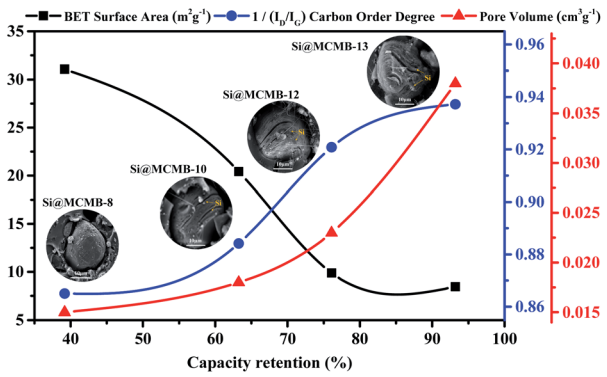

Fig. 9 Correlation between capacity retention rate (at 0.2 A g^{-1}) and structural parameters of Si@MCMB composites.

embedded in the turbostratic carbon layer texture with good order degree, which form an efficient conductive network skeleton and ensure material integrity and stability. Finally, the relatively smaller specific surface area and abundant void volume improved together the stability of the SEI layer, thus exhibiting high first coulomb efficiency. The next step and focus of work would be to further improve the coating and embedding rate and the content of nano-Si, so as to optimize the cyclic stability and high specific capacity of the Si@MCMB anodes.

4. Conclusion

In this study, a series of Si@MCMB composites were adjusted by heat treatment temperature in the range of 800–1400 °C using mesophase pitch as soft carbon source. The Si@MCMB composite anodes carbonized at a higher temperature had a turbostratic carbon layer texture with ordered carbon layer stacking, rich pore structure and smaller specific surface area, which showed a good capacity retention rate. These results suggested the co-existing structure of turbostratic carbon arrays with abundant porosity from mesophase pith, effectively improved the structural mechanical stability and the cycling and rate performance of electrodes. Importantly, the controlled strategy of adjusting the soft carbon microstructure by the heat treatment temperature may be applied to high rate Si/C anode materials.

Author contributions

Juntao Du: conceptualization, methodology, data curation, writing – original draft, writing – review & editing. Jiangkai Ma: validation, data curation, writing – original draft, formal analysis. Zetao Liu: data curation, validation, investigation. Wenchao Wang: data curation, validation, investigation. Huina Jia: visualization, data curation, investigation. Minxin Zhang: investigation, supervision, funding acquisition. Yi Nie: supervision, project administration, funding acquisition, writing – review & editing.

Conflicts of interest

The authors declare that they have no known competing financial interests or personal relationships that could have appeared to influence the work reported in this paper.

Acknowledgements

This work was financially supported by the National Natural Science Foundation of China (Youth Science Foundation Program No. 21908206), the Grant. YLU-DNL Fund of China (No. 2021015), the Key Science and Technology Project of Henan Province, China (No. 202102210213) and the Scientific and Technological Achievements Transfer and Transformation Project of Chinese Academy of Sciences in Henan Province, China (No. 2021102).

References

1 Y. Qi, G. Wang, S. Li, T. Liu, J. Qiu and H. Li, *Chem. Eng. J.*, 2020, **397**, 125380.
2 X. Zhang, D. Kong, X. Li and L. Zhi, *Adv. Funct. Mater.*, 2019, **29**, 1806061.
3 L. Wang, J. Han, D. Kong, Y. Tao and Q. Yang, *Nano-Micro Lett.*, 2019, **11**, 5.
4 F. Wang, Z. Hu, L. Mao and J. Mao, *J. Power Sources*, 2020, **450**, 227692.
5 A. Bianco, Y. Chen, Y. Chen, D. Ghoshal, R. H. Hurt, Y. A. Kim, N. Koratkar, V. Meunier and M. Terrones, *Carbon*, 2018, **132**, 785–801.
6 J. Guo, D. Dong, J. Wang, D. Liu, X. Yu, Y. Zheng, Z. Wen, W. Lei, Y. Deng, J. Wang, G. Hong and H. Shao, *Adv. Funct. Mater.*, 2021, **31**, 2102546.
7 Z. Jin, Z. Cui, X. Long, M. Millan, G. Yuan, Z. Dong, Y. Cong, J. Zhang, Y. Li and X. Li, *J. Alloys Compd.*, 2021, **887**, 161357.
8 J. Zhang, M. Terrones, C. R. Park, R. Mukherjee, M. Monthioux, N. Koratkar, Y. S. Kim, R. Hurt, E. Frackowiak, T. Enoki, Y. Chen, Y. Chen and A. Bianco, *Carbon*, 2016, **98**, 708–732.
9 B. Wang, Y. Peng, F. Yuan, Q. Liu, L. Sun, P. Zhang, Q. Wang, Z. Li and Y. A. Wu, *J. Power Sources*, 2021, **484**, 229244.
10 S. Ghosh, U. Bhattacharjee, S. Patchaiyappan, J. Nanda, N. J. Dudney and S. K. Martha, *Adv. Energy Mater.*, 2021, **11**, 2100135.
11 B. Sun, Q. Zhang, H. Xiang, F. Han, W. Tang, G. Yuan, Y. Cong, C. Fan, A. Westwood and X. Li, *Energy Storage Mater.*, 2020, **24**, 450–457.
12 D. Wang, J. Zhou, Z. Li, J. Li, L. Hou and F. Gao, *Ionics*, 2019, **25**, 1531–1539.
13 Y. He, F. Han, F. Wang, J. Tao, H. Wu, F. Zhang and J. Liu, *Electrochim. Acta*, 2021, **373**, 137924.
14 J. Du, J. Ma, Z. Liu, W. Wang, H. Jia, M. Zhang and Y. Nie, *Mater. Lett.*, 2022, **315**, 131921.
15 D. Schuepfer, F. Badaczewski, J. Guerra-Castro, D. Hofmann, C. Heiliger, B. Smarsly and P. Klar, *Carbon*, 2020, **161**, 359–372.
16 L. Chen, Y. Fei, X. Fan and Z. Jiang, *J. Mater. Sci.*, 2017, **52**, 12663–12676.
17 T. Li, C. Wang, X. Liu, J. Zheng and H. Wang, *Fuel Process. Technol.*, 2005, **87**, 77–83.
18 L. Chen, X. Fan, Z. Jiang, T. Ouyang and Y. Fei, *Carbon*, 2016, **103**, 421–424.
19 M. Fang, T. Ho, J. Yen, Y. Lin, J. Hong, S. Wu and J. Jow, *Materials*, 2015, **8**, 3550–3561.
20 C. Zhu, Y. Zhang, Z. Ma, H. Wang and G. L. Sly, *Nanotechnology*, 2021, **32**, 85403.
21 H. Shin, J. Hwang, H. J. Kwon, W. Kwak, S. Kim, H. Kim and H. Jung, *ACS Sustainable Chem. Eng.*, 2020, **8**, 14150–14158.
22 X. Gong, B. Lou, R. Yu, Z. Zhang, S. Guo, G. Li, B. Wu and D. Liu, *Fuel Process. Technol.*, 2021, **217**, 106832.
23 D. Schüpfer, F. Badaczewski, J. Peilstöcker, J. Guerra-Castro, H. Shim, S. Firoozabadi, A. Beyer, K. Volz, V. Presser,

C. Heiliger, B. Smarsly and P. Klar, *Carbon*, 2021, **172**, 214–227.
24 C. Ma, Z. Wang, Y. Zhao, Y. Li and J. Shi, *J. Alloys Compd.*, 2020, **844**, 156201.
25 T. Pfaff, F. Badaczewski, M. Loeh, A. Franz, J. Hoffmann, M. Reehuis, W. Zeier and B. Smarsly, *J. Phys. Chem. C*, 2019, **123**, 20532–20546.
26 M. F. Hassan, M. A. Sabri, H. Fazal, A. Hafeez, N. Shezad and M. Hussain, *J. Anal. Appl. Pyrolysis*, 2020, **145**, 104715.
27 L. Xie, C. Tang, Z. Bi, M. Song, Y. Fan, C. Yan, X. Li, F. Su, Q. Zhang and C. Chen, *Adv. Energy Mater.*, 2021, **11**, 2101650.
28 Y. Qi, Y. Lu, L. Liu, X. Qi, F. Ding, H. Li, X. Huang, L. Chen and Y. Hu, *Energy Storage Mater.*, 2020, **26**, 577–584.
29 L. Hou, H. Zheng, R. Cui, Y. Jiang, Q. Li, X. Jiang, J. Gao and F. Gao, *Microporous Mesoporous Mater.*, 2019, **275**, 42–49.
30 I. Mochida, C. Ku, S. Yoon and Y. Korai, *J. Power Sources*, 1998, **75**, 214–222.
31 G. Nava, J. Schwan, M. G. Boebinger, M. T. McDowell and L. Mangolini, *Nano Lett.*, 2019, **19**, 7236–7245.
32 S. Guo, X. Hu, Y. Hou and Z. Wen, *ACS Appl. Mater. Interfaces*, 2017, **9**, 42084–42092.
33 F. Dou, Y. Weng, Q. Wang, G. Chen, H. Liu, L. Shi and D. Zhang, *Chem. Eng. J.*, 2021, **417**, 128122.
34 H. Fujimoto, *J. Power Sources*, 2010, **195**, 5019–5024.
35 B. Xing, H. Zeng, G. Huang, J. Jia, R. Yuan, C. Zhang, Q. Sun, Y. Cao, Z. Chen and B. Liu, *Electrochim. Acta*, 2021, **376**, 138043.
36 Y. Wang, S. Chou, J. H. Kim, H. Liu and S. Dou, *Electrochim. Acta*, 2013, **93**, 213–221.
37 X. Zhang, M. Wang, Y. Wang, S. Zhou, G. Yang, Y. Ren, Q. Wang, R. Zhang, J. Zheng, X. Lu, W. Yang and L. Chen, *Solid State Ionics*, 2021, **364**, 115637.
38 S. Chen, L. Shen, P. A. van Aken, J. Maier and Y. Yu, *Adv. Mater.*, 2017, **29**, 1605650.
39 J. Yang, Y. Wang, S. Chou, R. Zhang, Y. Xu, J. Fan, W. Zhang, H. Kun Liu, D. Zhao and S. Xue Dou, *Nano Energy*, 2015, **18**, 133–142.
40 M. Jeong, H. L. Du, M. Islam, J. K. Lee, Y. Sun and H. Jung, *Nano Lett.*, 2017, **17**, 5600–5606.
41 Y. Zhang, B. Li, B. Tang, Z. Yao, X. Zhang, Z. Liu, R. Gong and P. Zhao, *J. Alloys Compd.*, 2020, **846**, 156437.
42 H. Dong, X. Fu, J. Wang, P. Wang, H. Ding, R. Song, S. Wang, R. Li and S. Li, *Carbon*, 2021, **173**, 687–695.